BPA-Fr in femorally tumor-bearing mice were 7.6 and 7.8, respectively. Previous experimental and clinical studies suggested that these ratios have to be at least 3 (Barth et al., 1996). The values of T/B and T/S obtained in the present study fulfill the therapeutic requirements.

H.E. staining data revealed that CCS tumor tissues were histologically different from the surrounding normal tissues, as evidenced from Fig. 3A. Fig. 3B–D shows the results of immunostaining with anti-BPA MAb. Here, the presence of BPA can be detected by browny coloration of tissues. The accumulation of BPA indicated by brownish color was predominant in the tumor tissues over the surround normal tissues (Fig. 3B), and tumor tissues obtained without BPA administration (negative control) did not develop brownish color well (Fig. 3C), suggesting that BPA is likely to be distributed in a CCS-selective manner. Interestingly, BPA was detected mainly in intracellular regions of CCS as seen in the magnified photograph (Fig. 3D). This can be a strong indication of cellular uptake of BPA taking place even *in vivo* CCS-bearing animals. Further studies are warranted to determine whether melanin synthesis is related to the high accumulation of boron in CCS.

4. Conclusions

Biodistribution of boron after i.v. administration of BPA-Fr into newly established CCS-bearing nude mice was studied. The peak concentrations of boron in tumor varied from 45 to 74 ppm, depending on the animal models. The T/B and T/S ratios were 9.2 and 4.5 in dorsally tumor bearing model, and 7.6 and 7.8 in femorally tumor bearing model, respectively. Tumor-specific BPA distribution was microscopically observed in the intravenously BPA-Fr-given CCS-bearing mice through immunohistological examination. A preclinical BNCT trial using a CCS-bearing mouse will be a next issue to clarify whether BNCT using BPA-Fr can be a promising therapeutic option for the CCS.

Acknowledgments

This work was supported in part by a Grant-in-Aid for Scientific Research (No. 22591657) from Japan Society for the Promotion of Science.

References

Barth, R.F., Soloway, A.H., Fairchild, R.G., Brugger, R.M., 1992. BNCT for cancer-realities and prospects. Cancer 70, 2995–3007.

Barth, R.F., Soloway, A.H., Brugger, R.M., 1996. Boron neutron capture therapy of brain tumors: past history, current status and future potential. Cancer Invest. 14, 534–560.

Fujimoto, T., Andoh, T., Sudo, T., Fujita, I., Imabori, M., Moritake, H., Sugimoto, T., Sakuma, Y., Takeuchi, T., Sonobe, H., Epstein, A.L., Akisue, T., Kirihata, M., Kurosaka, M., Fukumori, Y., Ichikawa, H. Evaluation of BPA uptake in clear cell sarcoma (CCS) *in vitro* and development of an *in vivo* model of CCS for BNCT studies. Appl. Radiat. Isots., in press, doi:10.1016/j.apradiso.2011.02.006.

Kirihata, M., Asano, T., 2008. JP Patent Pending 2008-94729.

Mishima, Y., Honda, C., Ichihashi, M., Obara, H., Hiratsuka, J., Fukuda, H., Karashima, H., Kobayashi, T., Kanda, K., Yoshino, K., 1989. Treatment of malignant-melanoma by single thermal-neutron capture therapy with melanoma-seeking B-10-compound. Lancet 12, 388–389.

Moritake, H., Sugimoto, T., Asada, Y., Yoshida, A.M., Maehara, Y., Epstein, L.A., Kuroda, H., 2002. Newly established clear cell sarcoma (malignant melanoma of soft parts) cell line expressing melanoma-associated Melan-A antigen and overexpressing C-MYC oncogene. Cancer Genet. Cytogenet. 135, 48–56.

Nakagawa, N., 2006. Therapeutic effect of boron neutron capture therapy on malignant glioma: fundamental studies using C6 rat glioma models. Med. J. Kinki Univ. 31, 215–224.

Weiss, S.W., Goldblum, J.R., 2001. Enzinger and Weiss's Soft Tissue Tumors, fourth ed., pp. 1240–1250.

Yoshino, K., Suzuki, A., Mori, Y., Kakihana, H., Honda, C., Mishima, Y., Kobayashi, T., Kanda, K., 1989. Improvement of solubility of p-boronophenylalanine by complex formation with monosaccharides. Strahlenther. Onkol. 165, 127–129.

Applied Radiation and Isotopes 69 (2011) 1642–1645

Contents lists available at ScienceDirect

Applied Radiation and Isotopes

journal homepage: www.elsevier.com/locate/apradiso

Experimental verification of beam characteristics for cyclotron-based epithermal neutron source (C-BENS)

H. Tanaka [a,*], Y. Sakurai [a], M. Suzuki [a], S. Masunaga [a], T. Mitsumoto [b], K. Fujita [b], G. Kashino [a], Y. Kinashi [a], Y. Liu [a], M. Takada [c], K. Ono [a], A. Maruhashi [a]

[a] Research Reactor Institute, Kyoto University, Osaka 590-0494, Japan
[b] Sumitomo Heavy Industries Ltd., Tokyo 141-6025, Japan
[c] National Institute of Radiological Sciences, Chiba 263-8555, Japan

ARTICLE INFO

Available online 21 March 2011

Keywords:
Boron neutron capture therapy
Cyclotron-based neutron source
Epithermal beam
Multi-foil

ABSTRACT

A cyclotron-based epithermal neutron source has been developed for boron neutron capture therapy. This system consists of a cyclotron accelerator producing 1.1-mA proton beams with an energy of 30 MeV, a beam transport system coupled with a beryllium neutron production target, and a beam-shaping assembly (BSA) with a neutron collimator. In our previous work, the BSA was optimized to obtain sufficient epithermal neutron fluxes of $\sim 10^9$ cm^{-2} s^{-1} using a Monte Carlo simulation code. In order to validate the simulation results, irradiation tests using multi-foil activation at the surface of a gamma-ray shield located behind the collimator and water phantom experiments using a collimated epithermal neutron beam were performed. It was confirmed experimentally that the intensity of the epithermal neutrons was 1.2×10^9 cm^{-2} s^{-1}.

© 2011 Elsevier Ltd. All rights reserved.

1. Introduction

At the Kyoto University Research Reactor Institute (KURRI), clinical trials of boron neutron capture therapy (BNCT) have been performed using the Kyoto University Research Reactor (KUR) (Sakurai and Kobayashi, 2002). The operation of KUR was stopped from March 2006 to May 2010 because of the change to low-enriched nuclear fuel. Clinical trials were restarted in May 2010.

At KURRI, a cyclotron-based neutron source (C-BENS) has also been developed for clinical use. In our previous work, a beam-shaping assembly (BSA) was optimized to obtain a sufficient intensity of epithermal neutrons, with reduction of gamma-ray contamination and of fast neutron doses (Tanaka et al., 2009). The design-based C-BENS was manufactured and installed at KURRI in December 2008. We started neutron production tests in March 2009. As of December 2010, various irradiation physical characteristics, such as whole-body exposure and measurements of BSA activities for reduction of worker exposure, and also biological characteristics, using cells and mice, had mostly been evaluated. It is especially important to confirm the influence of high-energy neutrons because the neutron energy of the C-BENS is higher than that of KUR.

In this paper, in order to validate the simulation results, irradiation tests using multi-foils for detecting high-energy neutrons over several MeV, and using a water phantom for detecting thermal neutron distributions, were performed.

2. Materials and methods

2.1. Cyclotron-based epithermal neutron source

The C-BENS consists of a cyclotron accelerator, manufactured by Sumitomo Heavy Industries, Ltd. (Tokyo, Japan), which can produce a 1.1-mA proton beam with an energy of 30 MeV, a beam transport system, a BSA, a collimator assembly (CA), and an irradiation bed. A detailed description of the device features is given in Mitsumoto et al. (2010). The schematic layout of the CA and the BSA of the C-BENS is shown in Fig. 1. The CA can move backward to view the setting position of a patient through the collimator window; this backward movement is also used to measure the neutron spectrum under free-in-air conditions in order to establish neutron sources for treatment planning.

To reduce the heat input at the beryllium target, the proton beam was expanded using scanner magnets. Reactions between 30-MeV protons and the beryllium target emit high-energy neutrons, up to 28 MeV, in the 0 degree direction. The BSA can reduce the neutron energy from around 28 MeV to the epithermal energy region because lead and iron work as moderators with inelastic cross-sections, and aluminum and calcium fluoride work as shapers, with a total cross-section, including the valley of

* Corresponding author. Tel.: +81 72 451 2468.
E-mail address: h-tanaka@rri.kyoto-u.ac.jp (H. Tanaka).

0969-8043/$ - see front matter © 2011 Elsevier Ltd. All rights reserved.
doi:10.1016/j.apradiso.2011.03.020

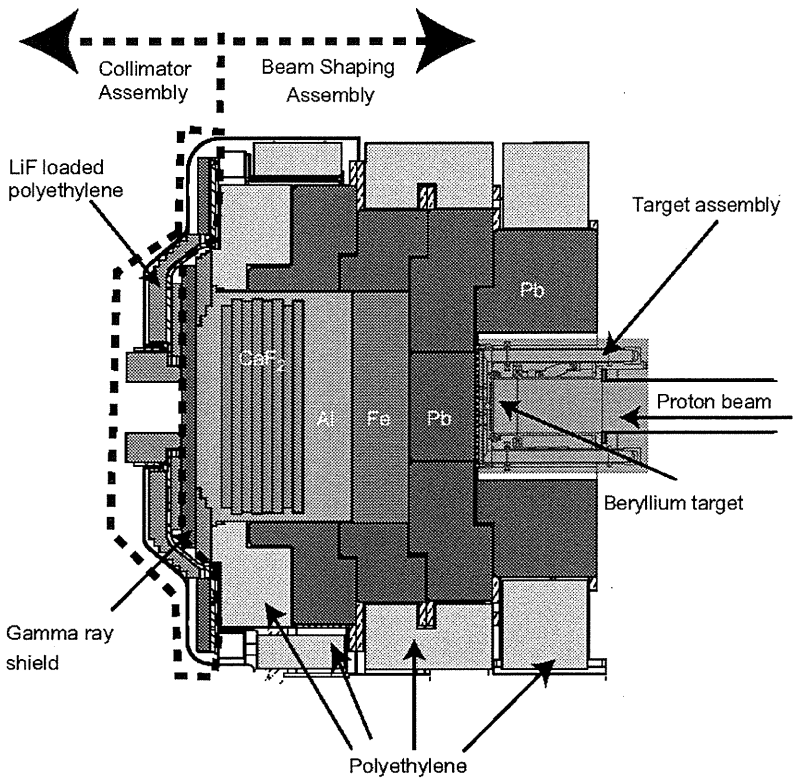

Fig. 1. Schematic layout of the beam-shaping assembly and collimator assembly of a cyclotron-based epithermal neutron source.

several tens of keV. Epithermal neutrons penetrating from the BSA go through a gamma-ray shield.

2.2. Multi-foil measurements

To measure the remaining high-energy neutrons over several MeV, multi-foils such as aluminum, nickel, and iron, which have a threshold energy, were placed at the center of the gamma-ray shield. After irradiation, the activities of the multi-foils were measured by a high-purity germanium detector (HP-Ge). To compare the results with the simulation results obtained with a MCNPX Monte Carlo code, the reaction rates for the multi-foils were derived from the equation below, using corrections such as cooling time: T_c, measuring time: T_m, and irradiation time: T; to correct the irradiation time precisely, variations in the proton current, expressed as $Q_i/\Delta t$, were taken into consideration:

$$R = \frac{\lambda C}{\varepsilon\gamma N_0 e^{-\lambda t_c}(1-e^{-\lambda t_m})\sum_{i-1}^{n}\left(\frac{Q_i}{\Delta t}(1-e^{-\lambda\Delta t})e^{-\lambda(n-i)\Delta t}\right)}, \quad (1)$$

where the constants $\lambda,\varepsilon,\gamma$, and C are the decay constant, detection efficiency, gamma-ray emission ratio, and total photo-peak counts, respectively.

2.3. Water phantom measurements

To measure the dose distributions of thermal neutrons and gamma-rays in a water phantom, a $30\times30\times20$ cm cubic water phantom was set in front of a collimator of diameter 25 cm. Gold wires and cadmium-covered gold wires were installed at the central axis, to detect thermal neutron flux. TLDs were also set at the central axis. To measure the thermal neutron flux in the lateral direction, gold wires and cadmium-covered gold wires were also installed at depths of 2 and 6 cm. After irradiation, the activities of the gold wires were measured by the HP-Ge. The cadmium ratio was used to estimate the thermal neutron flux.

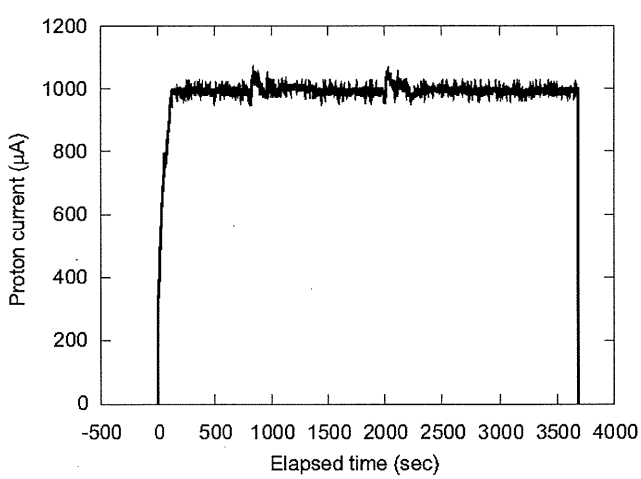

Fig. 2. Relationship between elapsed time and proton current detected at the beryllium target.

3. Results and discussion

3.1. Multi-foil measurements

Fig. 2 shows the typical relationship between elapsed time and proton current at the beryllium target. It was confirmed that the cyclotron can produce a stable proton current of up to ~1 mA for about 1 h. This is enough for use in clinical trials because the

epithermal neutron flux exceeds 10^9 cm^{-2} s^{-1} per proton current of 1 mA.

Fig. 3 shows the ratio of measured reaction rate to calculated reaction rate. Thermal/epithermal neutrons were measured by the reaction of ^{197}Au(n, γ)^{198}Au. To detect high-energy neutrons of the order of MeV, the reactions of ^{58}Ni(n,p)^{58}Co, ^{56}Fe(n,p)^{56}Mn, ^{27}Al(n, α)^{24}Na, and ^{58}Ni(n,2n)^{57}Ni with threshold energies of 2.8, 6.0, 7.2, and 13.5 MeV, respectively, were used. It was found that the ratio of the measured reaction rate to the calculated reaction rate was around 0.7 for the thermal/epithermal and high-energy regions.

According to the reference (Takata, 2010), the neutron spectra for a thick beryllium target using the cross-section data for ENDF/B-VII, and those using experimental data (Brede et al., 1989; Waterman et al., 1979), in the energy range from 17 to 35 MeV, were compared. This revealed that the cross-section data for ENDF/B-VII were higher than the experimental data. The overestimation of the cross-section data for ENDF/B-VII was a factor in the difference between the calculated and measured reaction rates.

Fig. 4 shows the relationship between the proton current at the beryllium target and the measured intensity of the epithermal neutron flux at the surface of a gamma-ray shield. This clearly confirmed good linearity between the proton current and the intensity of the epithermal neutron flux. Hence, the information on the proton current can be used to monitor neutron flux to decide on treatment times. The C-BENS can produce an epithermal flux intensity of up to 1.2×10^9 cm^{-2} s^{-1} with a proton current of 1 mA. In this paper, the energy range from 0.5 to 40 keV was defined as being the epithermal neutron range. The neutron fluxes for the thermal and fast regions were 5.0×10^6 and 6.0×10^7 cm^{-2} s^{-1}, respectively. The dose contaminations per epithermal neutron for fast neutrons and gamma-rays were 5.8×10^{-13} and 7.8×10^{-14} Gy cm^2, respectively.

3.2. Water phantom experiments

Fig. 5 shows the measured thermal neutron distribution in a water phantom compared with the calculated results. The collimator was 25 cm in diameter, which was the maximum size. The calculated

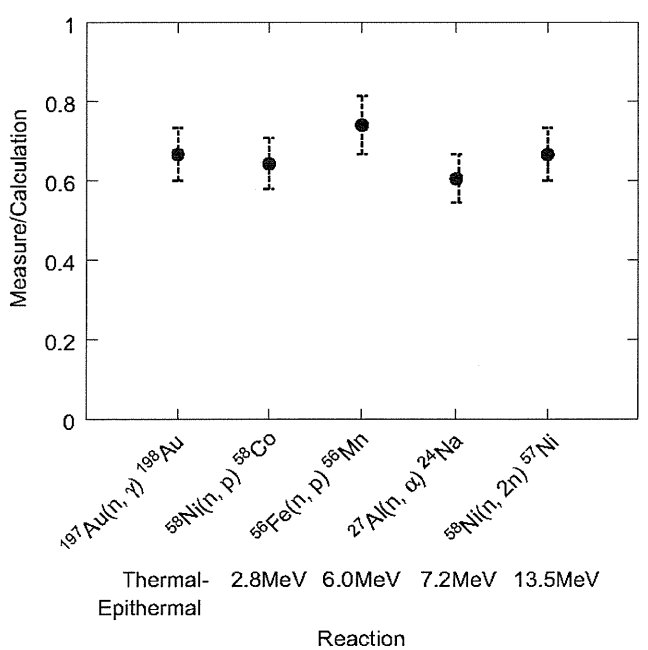

Fig. 3. Ratio of measured data from activities of multi-foils for detecting high-energy neutrons to calculated results using MCNPX.

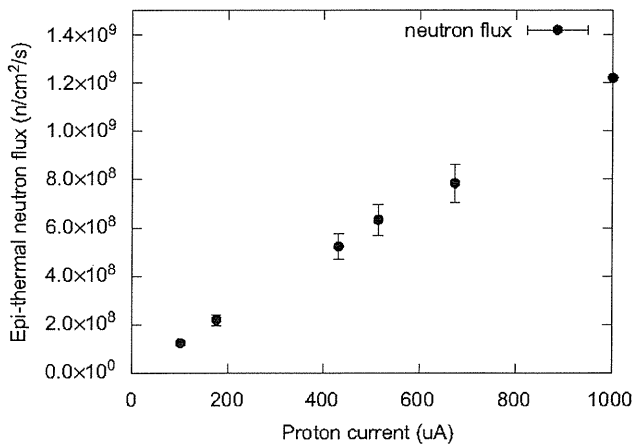

Fig. 4. Relationship between the proton current at the beryllium target and epithermal neutron flux at the surface of the gamma-ray shield.

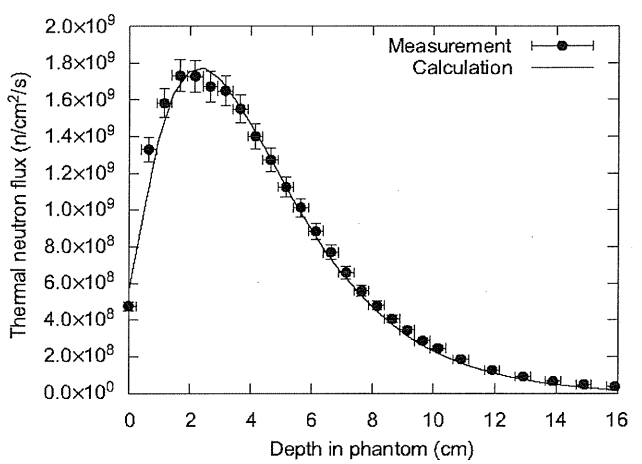

Fig. 5. Thermal neutron distributions in a water phantom at the central axis.

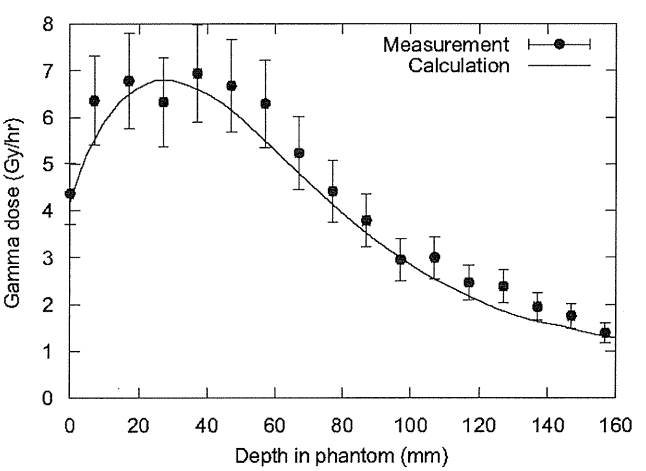

Fig. 6. Gamma-ray dose distributions in a water phantom at the central axis.

results were multiplied by the factor of 0.7 mentioned above. The calculated results multiplied by this factor were in good agreement with the measured data. The thermal neutron flux at a depth of 2 cm was 1.7×10^9 cm^{-2} s^{-1}.

Fig. 6 shows the gamma-ray dose distribution in a water phantom compared with the calculated results. The calculated

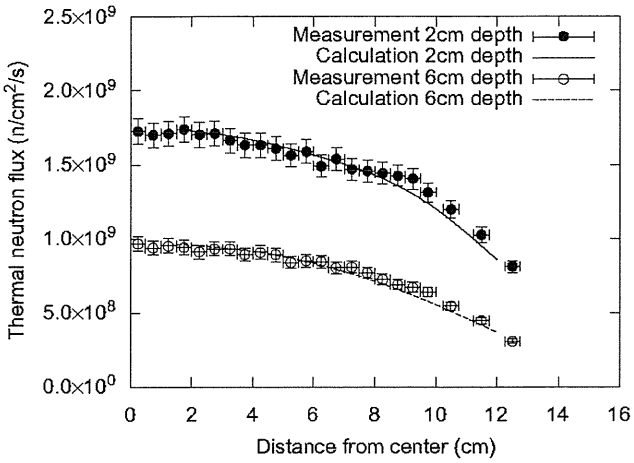

Fig. 7. Thermal neutron distributions in a water phantom in the lateral direction at depths of 2 and 6 cm.

results for the gamma-ray dose were also in good agreement with the measured data, within TLDs errors of less than 15%.

Fig. 7 shows the measured thermal neutron distribution in the lateral direction at depths of 2 and 6 cm. The measured data were also compared with the calculated results multiplied by the factor of 0.7. The calculated results were in good agreement with the measured data, except for distances beyond 8 cm from the center. It was thought that the difference between the measured data and the calculated results beyond 8 cm was caused by the effects of scattering from the walls, floor, and irradiation bed, which were not included in this calculation.

4. Conclusions

Experiments using multi-foils and a water phantom to validate the simulation results obtained with MCNPX code were performed. It was found that the simulation results for reaction rates caused by high-energy neutron and thermal neutron distributions in a water phantom were in good agreement with the measurement results. Good linearity between the proton current and epithermal neutrons at the surface of the gamma-ray shield was confirmed. Hence, the information on proton current can be used for measurements of neutron fluence in the determination of treatment times.

It was found from the experimental results that the intensity of the epithermal neutron flux at the center of the gamma-ray shield was 1.2×10^9 cm^{-2} s^{-1} under proton beam conditions of 1 mA. This value was about twice as large as that for the KUR reactor-based epithermal neutron source, which was used in over 300 clinical trials. Furthermore, C-BENS can produce stable operation with a proton current of 1 mA for 1 h. The use of C-BENS for clinical trials in the near future is desirable.

Acknowledgment

Part of this work was supported by the Association for Nuclear Technology in Medicine, Japan.

References

Brede, H.J., et al., 1989. Neutron yields from thick Be targets bombarded with deutrons and protons. Nucl. Instrum. Methods Phys. Res. A 274, 332–344.

Mitsumoto, T., et al., 2010. Cyclotron-based neutron source for BNCT. In: International Congress on Neutron Capture Therapy, pp. 519–522.

Sakurai, Y., Kobayashi, T., 2002. The medical-irradiation characteristics for neutron capture therapy at the heavy water neutron irradiation facility of Kyoto University Research Reactor. Med. Phys. 29 (10), 2328–2337.

Takata, T., 2010. Study on effective production of accelerator based neutron irradiation field for boron neutron capture therapy, Ph.D. Thesis, Kyoto University.

Tanaka, H., et al., 2009. Characteristics comparison between a cyclotron-based neutron source and KUR-HWNIF for boron neutron capture therapy. Nucl. Instrum. Methods Phys. Res. B 267, 1970–1977.

Waterman, F.M., et al., 1979. Neutron spectra from 35 and 46 MeV protons, 16 and 28 MeV deutrons, and 44 MeV ^{3}He ions on thick beryllium. Med. Phys. 6 (5), 432–435.

Applied Radiation and Isotopes 69 (2011) 1862–1865

Contents lists available at ScienceDirect

Applied Radiation and Isotopes

journal homepage: www.elsevier.com/locate/apradiso

Study on optimization of multiionization-chamber system for BNCT

T. Fujii [a,*], H. Tanaka [b], A. Maruhashi [b], K. Ono [b], Y. Sakurai [b]

[a] Kyoto University, Graduate School of Engineering, Yoshidahonmachi, sakyo-ku, Kyoto 606-8501, Japan
[b] Research Reactor Institute, Kyoto University, Asashiro-nishi 2-1010, Kumatori-cho, Osaka 590-0494, Japan

ARTICLE INFO

Available online 3 April 2011

Keywords:
Ionization-chamber
Accelerator-based neutron source
Beam monitor

ABSTRACT

In order to monitor stability of doses from the four components such as thermal, epi-thermal, fast neutron and gamma-ray during BNCT irradiation, we are developing a multiionization-chamber system.

This system is consisted of four kinds of ionization chamber, which have specific sensitivity for each component, respectively. Since a suitable structure for each chamber depends on the energy spectrum of the irradiation field, the optimization study of the chamber structures for the epi-thermal neutron beam of cyclotron-based epi-thermal neutron source (C-BENS) was performed by using a Monte Carlo simulation code "PHITS" and suitable chamber-structures were determined.

© 2011 Elsevier Ltd. All rights reserved.

1. Introduction

In irradiation fields of BNCT, many radiation components such as thermal (−0.5 eV), epi-thermal (0.5 eV–40 keV) and fast (40 keV-) neutron, and gamma-ray exist. Considering that the biological effectiveness of those components are different, accurate evaluation methods at real-time regarding the doses from 4-components have to be established for the quality assurance of BNCT. Based on this background, we suggested a "multiionization-chamber system" to monitor the stability of doses from the 4-components at real time during the irradiation. In this system, four kinds of ionization chambers (IC) having specific response for each component, are used in current mode. They are preferred to be small enough to have negligible effect on the beam, when placed at the edge of the beam collimator in the BNCT facility.

To complete this system, the structural optimizations of each IC for wall material, wall thickness and gas, are necessary for every irradiation fields. In this paper, the optimization study for the epi-thermal neutron spectrum of the cyclotron-based epi-thermal neutron source (C-BENS) in Kyoto University Research Reactor Institute (KURRI) is reported.

2. Material and methods

The optimization study was performed by using a Monte Carlo simulation code PHITS "Particle Heavy Ion Transport code System". This code can treat all ion transports and their deposit energy distribution (Iwase and Niita, 2002). The ionization chambers were modeled based on 2cc-chamber of the IC-17 series manufactured by Far West Technology (FWT). Combinations of each IC considered in this study is shown in Table 1.

For the IC of gamma-ray component (Gamma-IC), the surveys were performed for wall materials such as graphite (G), magnesium (Mg) and aluminum (Al), and gases such as argon (Ar) and carbon dioxide (CO_2). For the IC of thermal component in neutron (Thermal-IC), the surveys were performed for silicon nitride wall (Si_3N_4) and nitrogen gas (N_2) to enhance thermal response via $^{14}N(n,p)$ reaction. For the IC of epi-thermal component (Epi-IC), polyethylene wall (Poly) was selected as the effective moderator from epi-thermal to thermal, and N_2 gas was selected in the same way as on Thermal-IC. In addition, the sensitization in case that ^{10}B is coated at 1.8 μm thickness on inner wall was investigated for Epi-IC. For the IC of fast component (Fast-IC), Poly wall and methane gas (CH_4) were selected to enhance fast response via recoil proton generated in wall and gas.

The optimization surveys for wall thickness were performed from 0 to 10 mm in 1 mm increment, for Gamma-IC, Thermal-IC, and Fast-IC. As for Epi-IC, the survey was performed from 0 to 100 mm in 10 mm increment to confirm the thermalization of epi-thermal neutron in Poly-wall. The IC responses were evaluated as the electric-currents (hereinafter called the current) generated from respective components.

In the PHITS-simulation, all ICs were handled in the same manner. The energy deposited in gas by charged particle (proton, electron, alpha etc.) is calculated with a tally called Deposit Tally [T-deposit]. The unit of output obtained in a tally is MeV/cm^3, which can be converted into number of electron-ion pairs by using the gas volume in the chamber and its W-value for mainly generated-particles needed to create such a pair (ICRU, 1979).

* Corresponding author. Tel./fax: +81 72 451 2604.
E-mail address: f.takaaki@ft7.ecs.kyoto-u.ac.jp (T. Fujii).

0969-8043/$ - see front matter © 2011 Elsevier Ltd. All rights reserved.
doi:10.1016/j.apradiso.2011.03.031

Table 1
Combinations of ionization chamber.

IC-type	Wall (Gas)	Wall thickness (mm) (Increment (mm))
Gamma-IC	G/Mg/Al (Ar/CO_2)	0–10 (1)
Thermal-IC	$Si_3N_4(N_2)$	0–10 (1)
Epi-IC	$Poly(N_2)+{}^{10}B$	0–100 (10)
Fast-IC	$Poly(CH_4)$	0–10 (1)

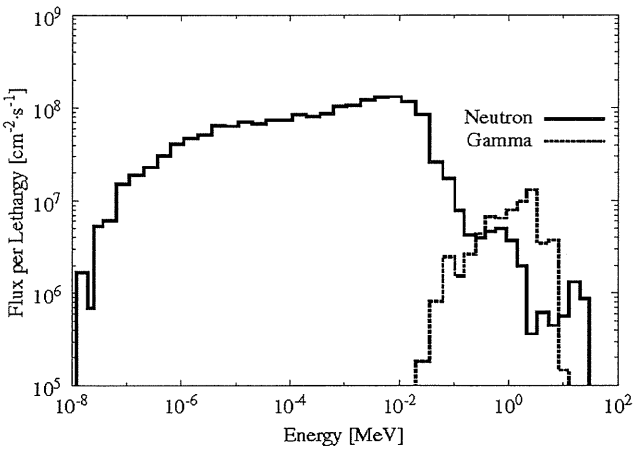

Fig. 1. Energy spectra of epi-thermal neutron beam (solid line: neutron and dash line: gamma-ray).

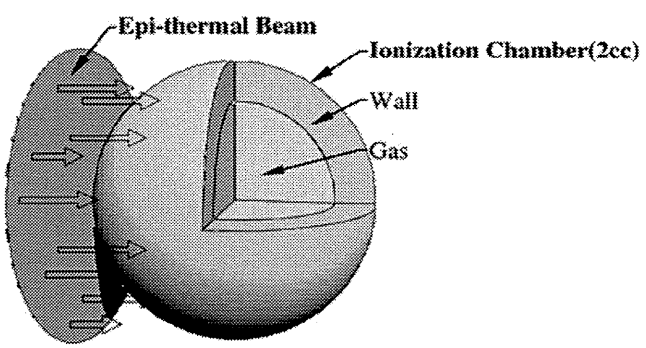

Fig. 2. Geometry in PHITS calculation.

The number of electron per second, namely current, is finally obtained using the beam intensity and the elementary charge in gas. The energy spectrum data obtained at the collimator aperture of C-BENS (Tanaka and Sakurai, 2009) were set as the source data of neutron and gamma-ray. The energy spectra of the epi-thermal neutron beam at C-BENS used in this study are shown in Fig. 1 (solid line: neutron and dash line: gamma-ray). The neutron spectrum was divided into three components (thermal, epi-thermal and fast), and each component was used as a neutron source for its energy range. The geometry used in the PHITS is shown in Fig. 2. A chamber is placed facing with the surface source for gamma-ray and neutron from C-BENS. The directionality of the source is assumed to be parallel. The diameter of the surface source is the same as that of the chamber outside-wall in order to reduce the calculation time.

3. Simulation results

The calculated currents for all ICs were in the pA-level, which is a sufficiently measurable level using an ammeter.

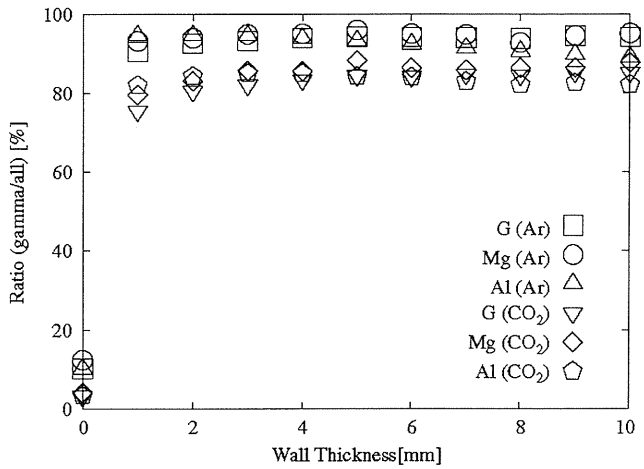

Fig. 3. The relationship between gamma-ray ratio and wall thickness.

3.1. Gamma-IC

Chambers filled with argon gas showed higher sensitivity ratio than that of CO_2 gas for gamma component by 20%, since deposited energy from charged particles produced by reaction with fast component is suppressed by the low cross section in argon.

This shows that a Graphite wall of 4-mm thickness and argon gas is the best combination in the three wall materials. The ratio of gamma-ray to all components is approximately 95% in the electric current using this combination (see Fig. 3.)

3.2. Thermal-IC

It is difficult to obtain a higher current compared to the other three components. Because, there is low thermal component at C-BENS originally (see Fig. 4(a)). The ratio of thermal to all components did not depend on the wall thickness but mainly depend on gas type. So the optimum thickness of Si_3N_4 wall is between 1 and 10 mm in terms of this study, and the ratio of thermal to all components at these thicknesses is approximately 20%.

3.3. Epi-IC

The 30 mm thick of Poly generates the peak electric-current for epi-thermal component due to the reaction with N_2 gas and neutron moderated in wall, and the ^{10}B-coated chamber generates two order higher current than the no-coated one due to the large energy-transfer by alpha and lithium particle from $^{10}B(n, \alpha)^7Li$ reaction (see Fig. 4(b)). This means that the wall also plays a role as epi-thermal moderator, and the thermalized epi-thermal component reacts with the coating ^{10}B and the N_2 gas. The ratio of epi-thermal to all components at 30 mm is approximately 96%.

3.4. Fast-IC

The current derived from epi-thermal component is dominant in smaller wall thickness, and it decreases with increases in wall thickness (see Fig. 4(c)). The ratio of fast to all components at 10 mm is approximately 50%.

4. Experimental results

Experiments were performed at the C-BENS facility to verify the PHITS simulations and currents calculation methods. As the

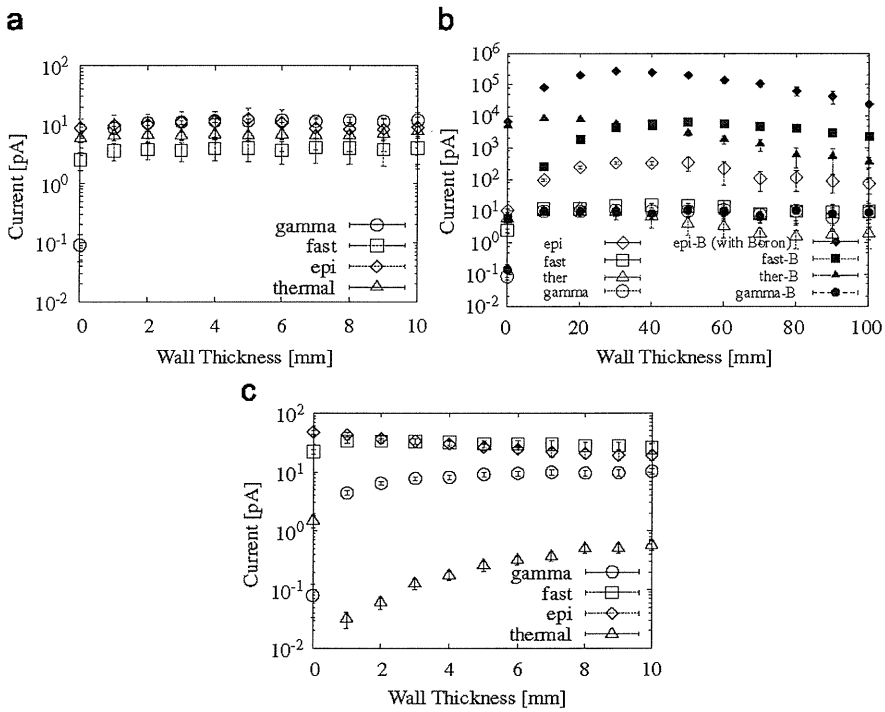

Fig. 4. Comparison of current for each neutron chamber: (a) thermal-IC, (b) epi-IC, and (c) fast-IC.

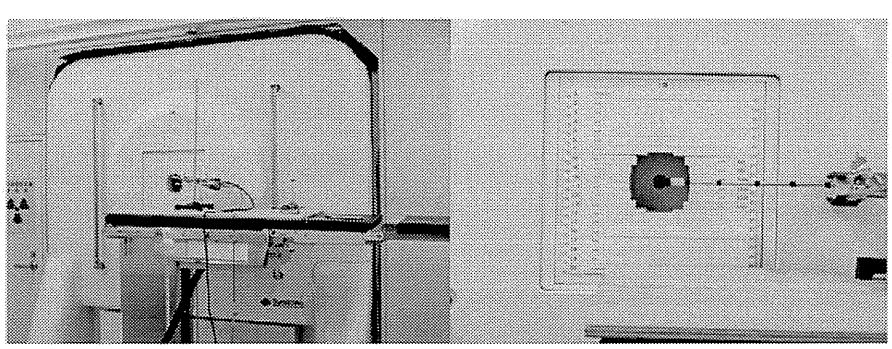

Fig. 5. Experimental settings for the ionization chambers at C-BENS.

Table 2
Comparison for the obtained currents at C-BENS between the experiments and PHITS-simulations.

IC-type	PHITS (pA)	Exp (pA)	PHITS/Exp
Fast-IC (1cc)	26.6 ± 2.0	28 ± 2	0.95 ± 0.15
Gamma-IC (2cc)	30.1 ± 2.5	42 ± 3	0.71 ± 0.13

Gamma-IC and Fast-IC, commercially available chambers (IC-17G(2cc) and IC-17P(1cc) manufactured by FWT) were used. Fig. 5 shows the experimental settings at the C-BENS facility. The ionization chambers were placed at the center of the epi-thermal beam collimator (Fig. 5). Neutron beam spectrum is the same configuration of the simulation source.

Table 2 shows the results of current comparison between experiments and calculation using PHITS. The experiment and the simulation results were in good agreement for Fast-IC chambers within 5%. For Gamma-IC, however, calculation showed 30% disagreement compared with experiments. The differences between calculation and experiment seems to derive from charge estimation methods or gamma-ray data we used.

5. Conclusions

The optimization surveys for wall and gas of ICs using multi-ionization chamber system were performed for the C-BENS facility. For Gamma-IC, it is concluded that graphite wall of 4 mm thickness and argon gas is the best combination. The ratio of gamma-ray to all components is approximately 95% using this combination.

For Thermal-IC, the optimum thickness of IC wall is 1–10 mm of Si_3N_4 in terms of this study due to independence from wall thickness. The ratio of thermal to all components at these thicknesses is approximately 20%. For Epi-IC, 30 mm of Poly generates the peak of current for epi-thermal component. But, this size of Poly increases thermal component at 9% in the

neutron beam when the IC is placed at the edge of the collimator aperture for the C-BENS side. The optimum thickness of Poly was determined to 10 mm in this study, because the ratio of epithermal to all components is large (approximately 90%) enough to get the sufficient current and the increase of thermal components is negligible by the Poly of this thickness. For Fast-IC, the optimum thickness of Poly-wall is 10 mm, and the ratio of fast to all components is approximately 50%.

As works in the near future, response factors for 4-components of 4-ICs have to be determined, respectively, based on experimental results from several fields having different neutron spectra, and we will finally make the optimized-ICs and complete the multiionization-chamber system for C-BENS.

References

ICRU, 1979. Average energy required to produce an ion pair. ICRU Report 31, Bethesdas, MD.

Iwase, H., Niita, K., 2002. Development of general-purpose particle and heavy ion transport Monte Carlo code. J. Nucl. Sci. Technol. 39 (11), 1142–1151.

Tanaka, H., Sakurai, Y., 2009. Improvement of dose distribution in phantom by using epithermal neutron source based on the Be(p,n) reaction using a 30 MeV proton cyclotron accelerator. Appl. Radiat. Isotop. 67, 258–261.

Examination of ^{11}C-Methionine Metabolism by the Standardized Uptake Value in the Normal Brain of Children

Takashi Nagata, Naohiro Tsuyuguchi, Takehiro Uda, Yuzo Terakawa, Toshihiro Takami, and Kenji Ohata

Department of Neurosurgery, Osaka City University Graduate School of Medicine, Osaka, Japan

The aim of this study was to determine the uptake of L-[methyl-^{11}C]-methionine (^{11}C-MET) in the normal brain of patients younger than 20 y, to facilitate more accurate diagnoses in young patients. **Methods:** Eighty-two patients were categorized into 4 groups according to their age. They underwent ^{11}C-MET PET, and a standardized uptake value (SUV) was determined for different brain regions including the frontal lobe, parietal lobe, cerebellum, and brain stem. **Results:** Compared with all other parts of the brain, the cerebellum had the highest SUV. A tendency for a positive relationship between SUV and age was found in all regions, and a significant relationship with SUV was found in the frontal lobe and cerebellum. **Conclusion:** The character of SUV in the normal brains of children is different from that of adults, and these normal SUV data will play an important role as a critical reference value.

Key Words: ^{11}C-methionine PET; normal accumulation; standardized uptake value; children

J Nucl Med 2011; 52:201–205
DOI: 10.2967/jnumed.110.082875

The tracer L-[methyl-^{11}C]-methionine (^{11}C-MET) is useful for PET in neurooncology (*1,2*), making it possible to assess the characteristics of lesions that could not be diagnosed by other means (*1,3–7*). ^{11}C-MET uptake is also informative about the malignancy of lesions, as is ^{18}F-FDG PET (*6,7*). For younger patients, it is critical to get accurate information about lesions, such as the degree of malignancy and extent of lesions, as early as possible. Therefore, it is essential to have an accurate understanding of ^{11}C-MET PET data. To date, ^{11}C-MET PET has been interpreted mainly using the lesion-to-normal (L/N) ratio—comparison between ^{11}C-MET uptake in the lesion and that in the corresponding normal region in the contralateral hemisphere (*8–10*). In cases of a highly malignant lesion, it would be relatively easy to point out where the lesion is, but when the disease has low malignancy, it may be difficult because interpretation of the result is semiquantitative. Thus, an absolute index is desirable. Uda et al. determined the normal ^{11}C-MET uptake and extent of variation (*11*), but there is no report about normal uptake among children. In the current study, we evaluated normal ^{11}C-MET uptake in persons younger than 20 y.

Received Aug. 31, 2010; revision accepted Oct. 21, 2010.
For correspondence or reprints contact: Takashi Nagata, 1-4-3 Asahi-machi, Abeno-ku, Osaka, Japan 545-8585.
E-mail: tnagatam.0222512.ns@gmail.com
COPYRIGHT © 2011 by the Society of Nuclear Medicine, Inc.

MATERIALS AND METHODS

Patients

Between February 1994 and May 2008, 1,228 patients underwent ^{11}C-MET PET at Osaka City University Hospital. Of these patients, 136 were 20 y or younger. Exclusion criteria included the following: infiltrative grade II–IV neoplasm according to the World Health Organization classification (*12*), extramedullary or midline tumors greater than 20 mm in diameter (3 patients), edematous changes in the brain (3 patients), and history of radiation therapy or chemotherapy (48 patients). The remaining 82 patients (40 male and 42 female; mean age ± SD, 12.4 ± 6.1 y; range, 0–20 y), who were not taking any drugs that could influence brain metabolism, were divided into 4 groups according to their age: group 1, 0–5 y; group 2, 6–10 y; group 3, 11–15 y; and group 4, 16–20 y. The standardized uptake value (SUV) of normal brains was examined according to age and each region, including the frontal lobe, parietal lobe, cerebellum, and brain stem.

The Ethics Committee of Osaka City University Graduate School of Medicine approved this PET study. Informed consent was obtained from all patients or their parents.

PET

PET was performed with an Eminence B PET scanner (Shimadzu); the spatial resolution was 4.5 mm (in full width at half maximum), and slice thickness was 5.6 mm. Scans were obtained parallel to the orbitomeatal line of the patients. After 4 h of fasting, ^{11}C-MET (6 MBq/kg) was injected intravenously over 30 s. After a transmission scan was obtained, a static scan of 10 min was begun 20 min after injection.

Imaging Analysis

Two experienced nuclear medicine radiologists interpreted the scans. The PET images were reconstructed by measured attenuation correction. In both analyses, the region of interest (ROI) was placed manually in the axial plane within the frontal cortex, parietal cortex, cerebellum, and brain stem (Fig. 1). The ROIs of these regions, except for the brain stem, were demarcated manually within the lateral side of the gray matter by reference to the MRI data. In the brain stem, the ROI was placed over the whole

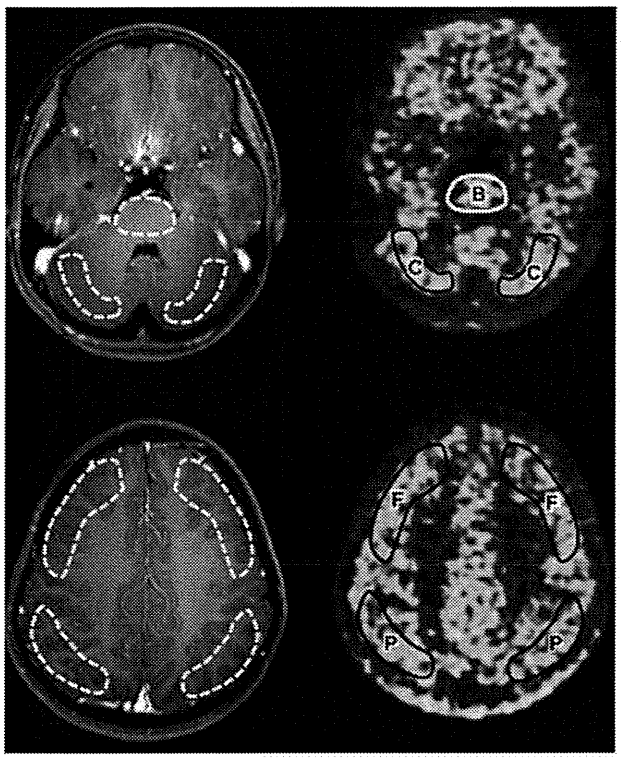

FIGURE 1. Sample of ^{11}C-MET PET images. ROIs were taken manually in axial plane. Coregistration between MR images and PET scans is adequate. B = brain stem; C = cerebellum; F = frontal cortex; P = parietal cortex.

brain stem at the middle pons level. Mean pixel counts in the ROIs were normalized to SUV using the subject's body weight with the following equation: SUV = ([mean pixel count/pixel volume]/[injected radioisotope activity/body weight]) × calibration factor.

Statistical Analysis

The differences between each part of the brain were analyzed in every group. The sample consisted of 54 patients for whom we had all SUV data, including the right frontal lobe, right parietal lobe, right cerebellum, and brain stem. Statistical analysis was performed by non–repeated-measures ANOVA, with post hoc tests corrected using Bonferroni and Student–Newman–Keuls analysis.

The relationship between SUV and age was analyzed in every part of the brain with linear regression and Spearman correlation tests. The samples used in these analyses were 158 frontal hemispheres (79 right hemispheres and 79 left hemispheres), 118 parietal hemispheres (59 right hemispheres and 59 left hemispheres), 156 cerebellar hemispheres (77 right hemispheres and 79 left hemispheres), and 62 brain stems. In all statistical analyses, significance was defined as a P value less than 0.05.

RESULTS

Frontal Lobe

SUVs (mean ± SD) in the frontal lobe were 1.133 ± 0.295 and 1.088 ± 0.379 in group 1, 1.067 ± 0.264 in group 2, 1.101 ± 0.268 in group 3, and 1.199 ± 0.258 in group 4 (Table 1). A significant linear regression between SUV and age ($P = 0.0282$) was found (Fig. 2).

Parietal Lobe

SUVs (mean ± SD) in the frontal lobe were 1.149 ± 0.290 and 1.052 ± 0.399 in group 1, 1.114 ± 0.209 in group 2, 1.122 ± 0.220 in group 3, and 1.235 ± 0.243 in group 4 (Table 1). Significant differences between groups 1 and 4 ($P < 0.01$) were found, but no significant linear regression between SUV and age ($P = 0.396$) was found (Fig. 2).

Cerebellum

SUVs (mean ± SD) in the frontal lobe were 1.312 ± 0.309 and 1.145 ± 0.347 in group 1, 1.319 ± 0.345 in group 2, 1.327 ± 0.301 in group 3, and 1.394 ± 0.251 in group 4 (Table 1). Significant differences between groups 1 and 2 ($P < 0.05$), groups 1 and 3 ($P < 0.01$), and groups 1 and 4 ($P < 0.01$) were found. A significant linear regression between SUV and age ($P = 0.00197$) was also found (Fig. 2).

Brain Stem

SUVs (mean ± SD) in the frontal lobe were 1.245 ± 0.306 and 1.096 ± 0.367 in group 1, 1.222 ± 0.165 in group 2, 1.268 ± 0.3422 in group 3, and 1.298 ± 0.265 in group 4 (Table 1). No statistically significant difference between SUV and age was found (Fig. 2).

Comparison Between Each Part of Brain

Fifty-four of the 82 patients were analyzed, and significant differences between the frontal lobe and cerebellum ($P < 0.01$), frontal lobe and brain stem ($P < 0.01$), parietal lobe and cerebellum ($P < 0.05$), and parietal lobe and brain stem ($P < 0.05$) were found (Fig. 3). In group 3, significant

TABLE 1
SUV in Each Part of Brain in Every Group

	Frontal lobe		Parietal lobe		Cerebellum		Brain stem	
Group	*n*	Mean ± SD	*n*	Mean ± SD	*n*	Mean ± SD	*n*	Mean ± SD
1	36	1.088 ± 0.379	30	1.052 ± 0.399	35	1.145 ± 0.347	11	1.096 ± 0.367
2	14	1.067 ± 0.264	12	1.114 ± 0.209	12	1.319 ± 0.345	6	1.222 ± 0.165
3	46	1.101 ± 0.268	28	1.122 ± 0.220	46	1.327 ± 0.301	20	1.268 ± 0.3422
4	62	1.199 ± 0.258	48	1.235 ± 0.243	63	1.394 ± 0.251	25	1.298 ± 0.265
Total	158 (right, 79; left, 79)	1.133 ± 0.295	118 (right, 59; left, 59)	1.149 ± 0.290	156 (right, 77; left, 79)	1.312 ± 0.309	62	1.245 ± 0.306

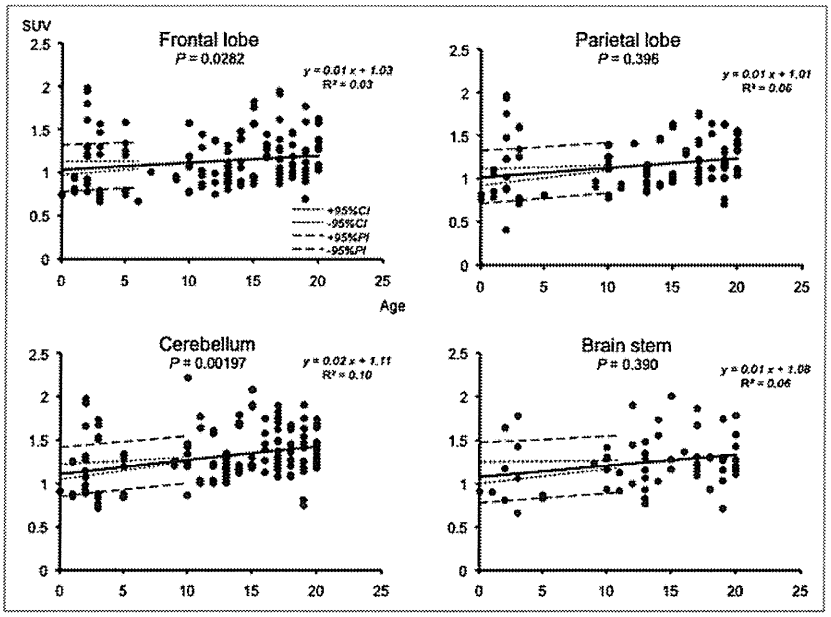

FIGURE 2. Regression and scatterplots for analysis of age-associated SUV change in frontal lobe, parietal lobe, cerebellum, and brain stem. In all parts of brain, positive linear regression was found, but *P* value of regression coefficient was statistically significant only in frontal lobe and cerebellum.

differences between the frontal lobe and cerebellum ($P < 0.01$) and frontal lobe and brain stem ($P < 0.01$) were found. But in groups 1, 2, and 4, there was no significant difference between each part of the brain (Fig. 4).

DISCUSSION

^{11}C-MET PET has been used for the description of lesions and for less invasive evaluation of malignancy. Many papers show that PET is more sensitive and specific than MRI in detecting intracranial tumors (*6,9,10*), because PET can detect amino acid metabolism in various cells directly. In general, amino acid metabolism is low in normal brain tissue and high in tumor tissue. According to this difference in ^{11}C-MET accumulation, ^{11}C-MET PET can display clear contrast images for lesions. Therefore, ^{11}C-MET PET would be an informative modality for detecting the boundary between an active lesion and normal brain tissue (*6*). Some reports have also described ^{18}F-FDG PET as being helpful in assessing the degree of malignancy (*3–6*), and ^{11}C-MET PET is also associated with malignancy and may provide valuable information on clinical tumor aggressiveness and prognosis (*6,7,13*).

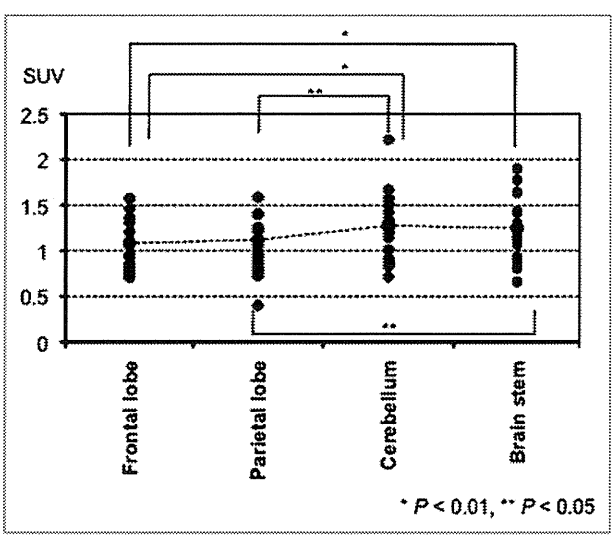

FIGURE 3. SUV in different parts of brain among patients aged 0–20 y. Significant differences between frontal lobe and cerebellum, frontal lobe and brain stem, parietal lobe and cerebellum, and parietal lobe and brain stem were observed.

In general, ^{11}C-MET PET images have been evaluated mainly by using an L/N ratio that compares ^{11}C-MET uptake in the lesion with that in the corresponding normal region in the contralateral hemisphere (*8–10*). Because the reference normal tissue will influence the result of the L/N ratio as a denominator, it is important that an appropriate location be chosen for the ROI used to calculate the normal reference value (*14*).

There are variations in normal ^{11}C-MET accumulation for each part of the brain and variation between different ages (*11*). The reliability of the L/N ratio will, then, decline when uptake in the lesion is not so high. In addition, in the case of tumors near the midline or brain stem, it will be difficult to set normal ROIs in the contralateral region. Therefore, it is important to know the absolute amount of SUVs in the normal brain.

In a previous study, Uda et al. reported the SUV in the normal adult brain (*11*), and such data are an important indicator of amino acid metabolism. To date, there has been no report about normal uptake of ^{11}C-MET in brains throughout development, including infancy, childhood, and

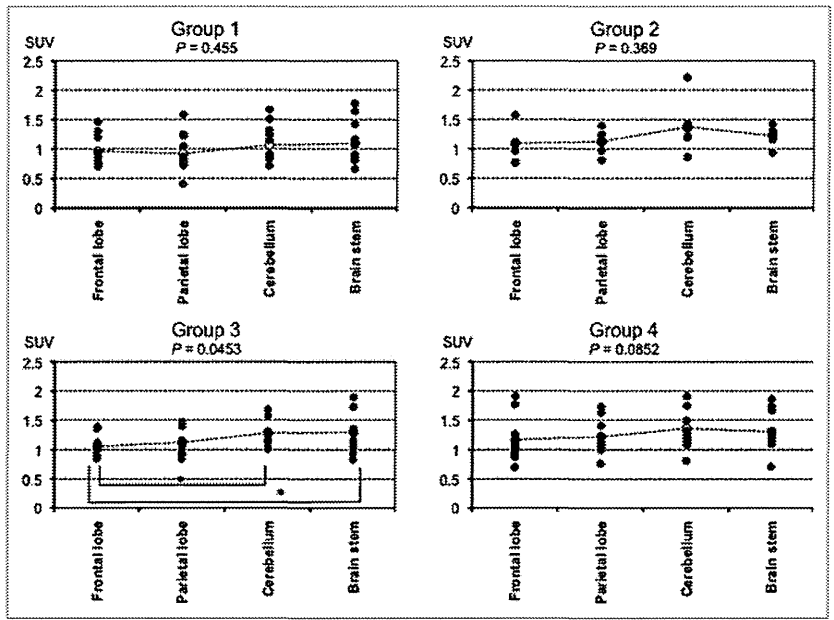

FIGURE 4. SUV in different brain parts in every group. In group 1, SUV was highest in brain stem, followed by cerebellum, but significant difference was not observed. In group 2, SUV was highest in cerebellum but also was not statistically significantly different from other regions. In group 3, significant differences between frontal lobe and cerebellum and frontal lobe and brain stem were found. In group 4, although SUV was highest in cerebellum, difference was not statistically significant. *$P < 0.01$.

young adulthood. If standard amino acid metabolism varies by age, the SUV may be a more suitable indicator than the L/N ratio in ^{11}C-MET PET.

In previous reports, O'Tuama et al. showed a significant age-dependent decline of ^{11}C-MET uptake in maturing adults (*15*), and Uda et al. also reported a slightly negative linear regression, although no statistically significant difference was observed (*11*). The reason for this age-associated decline in ^{11}C-MET uptake was explained as a developmental decline in the activity of the neutral amino acid transporter of the blood–brain barrier (*15*). In the present study, we found that uptake of ^{11}C-MET in all parts of the brain we studied gradually increased with age until 20 y, possibly reflecting high activity of the neutral amino acid transporter and brain protein synthesis to meet the needs of brain metabolism. These results suggest that the brains of younger persons are immature and still developing.

On the other hand, ^{18}F-FDG PET, the local cerebral metabolic rate for glucose, is higher in infants at 3–5 mo old (*16,17*). This tendency is different from our result in ^{11}C-MET PET because the metabolism of glucose represents not only the activity of neurocytes but also the activity of the neural network, including structures around synapses, whereas amino acid metabolism indicates the extent of protein synthesis. ^{11}C-MET uptake also increases linearly as the brain matures during young adulthood. After brain weight reaches a plateau, the uptake begins to decrease, reflecting developmental decline, as described in a previous report (*15*).

In each part of the brain, SUV was highest in the cerebellum in this population, similar to results reported for adult humans investigated by Uda et al. (*11*). The plasticity of synapses is important for motor learning (*18*), which is critically governed by the cerebellum. Activity of the neural network will increase amino acid metabolism in neurocytes, and this higher motor learning will continue for a lifetime. In addition, there is higher cell density in the cerebellum, especially in the granular cell layer, than is found in other brain regions. Therefore, total amino acid metabolism will increase. These are possible reasons for high accumulation in the cerebellum.

We obtained more reliable information about ^{11}C-MET SUV in normal brains, including age-associated and regional changes. This study provides useful information for clinical determinations such as operative indications, which are affected by the malignancy of the lesion.

When continuous long-term follow-up is necessary in some children and younger patients, information about normal metabolism variation associated with aging is useful in making judgments regarding the effectiveness of treatment, and thus it is essential to make accurate evaluations according to a patient's age and brain region.

CONCLUSION

The present study evaluated the accumulation of ^{11}C-MET and SUVs in the normal brain among children and young adults and found significant age-associated differences in some regions. To make more accurate evaluations in ^{11}C-MET PET, age-associated criteria will be necessary in children and young adults.

REFERENCES

1. De Witte O, Goldberg I, Wikler D, et al. Positron emission tomography with injection of methionine as a prognostic factor in glioma. *J Neurosurg.* 2001;95:746–750.
2. Kato T, Shinoda J, Oka N, et al. Analysis of ^{11}C-methionine uptake in low-grade gliomas and correlation with proliferative activity. *AJNR.* 2008;29:1867–1871.

3. Goldman S, Levivier M, Pirotte B, et al. Regional methionine and glucose uptake in high-grade gliomas: a comparative study on PET-guided stereotactic biopsy. *J Nucl Med.* 1997;38:1459–1462.
4. Kaschten B, Stevenaert A, Sadzot B, et al. Preoperative evaluation of 54 gliomas by PET with fluorine-18-fluorodeoxyglucose and/or carbon-II-methionine. *J Nucl Med.* 1998;39:778–785.
5. Levivier M, Massager N, Wikler D, et al. Use of stereotactic PET images in dosimetry planning of radiosurgery for brain tumors: clinical experience and proposed classification. *J Nucl Med.* 2004;45:1146–1154.
6. Pirotte BJ, Lubansu A, Massager N, et al. Clinical interest of integrating positron emission tomography imaging in the workup of 55 children with incidentally diagnosed brain lesions. *J Neurosurg Pediatr.* 2010;5:479–485.
7. Utriainen M, Metsahonkala L, Salmi TT, et al. Metabolic characterization of childhood brain tumors: comparison of F-18-fluorodeoxyglucose and C-11-methionine positron emission tomography. *Cancer.* 2002;95:1376–1386.
8. Terakawa Y, Tsuyuguchi N, Iwai Y, et al. Diagnostic accuracy of ^{11}C-methionine PET for differentiation of recurrent brain tumors from radiation necrosis after radiotherapy. *J Nucl Med.* 2008;49:694–699.
9. Tsuyuguchi N, Sunada I, Iwai Y, et al. Methionine positron emission tomography of recurrent metastatic brain tumor and radiation necrosis after stereotactic radiosurgery: is a differential diagnosis possible? *J Neurosurg.* 2003;98:1056–1064.
10. Tsuyuguchi N, Takami T, Sunada I, et al. Methionine positron emission tomography for differentiation of recurrent brain tumor and radiation necrosis after stereotactic radiosurgery: in malignant glioma. *Ann Nucl Med.* 2004;18:291–296.
11. Uda T, Tsuyuguchi N, Terakawa Y, Takami T, Ohata K. Evaluation of the accumulation of ^{11}C-methionine with standardized uptake value in the normal brain. *J Nucl Med.* 2010;51:219–222.
12. Louis DN, Ohgaki H, Wiestler OD, et al. The 2007 WHO classification of tumours of the central nervous system. *Acta Neuropathol.* 2007;114:97–109.
13. Kato T, Shinoda J, Nakayama N, et al. Metabolic assessment of gliomas using ^{11}C-methionine, [^{18}F] fluorodeoxyglucose, and ^{11}C-choline positron-emission tomography. *AJNR.* 2008;29:1176–1182.
14. Coope DJ, Cizek J, Eggers C, Vollmar S, Heiss WD, Herholz K. Evaluation of primary brain tumors using ^{11}C-methionine PET with reference to a normal methionine uptake map. *J Nucl Med.* 2007;48:1971–1980.
15. O'Tuama LA, Phillips PC, Smith QR, et al. L-methionine uptake by human cerebral cortex: maturation from infancy to old age. *J Nucl Med.* 1991;32:16–22.
16. Suhonen-Polvi H, Ruotsalainen U, Kinnala A, et al. FDG-PET in early infancy: simplified quantification methods to measure cerebral glucose-utilization. *J Nucl Med.* 1995;36:1249–1254.
17. Chugani HT, Phelps ME. Maturational changes in cerebral function in infants determined by ^{18}F-FDG positron emission tomography. *Science.* 1986;231:840–843.
18. Boyden ES, Katoh A, Raymond JL. Cerebellum-dependent learning: the role of multiple plasticity mechanisms. *Annu Rev Neurosci.* 2004;27:581–609.

J Neurooncol (2011) 103:175–185
DOI 10.1007/s11060-010-0376-5

LABORATORY INVESTIGATION - HUMAN/ANIMAL TISSUE

Convection enhanced delivery of carboranylporphyrins for neutron capture therapy of brain tumors

Shinji Kawabata · Weilian Yang · Rolf F. Barth · Gong Wu · Tianyao Huo · Peter J. Binns · Kent J. Riley · Owendi Ongayi · Vijay Gottumukkala · M. Graça H. Vicente

Received: 1 February 2010 / Accepted: 19 August 2010 / Published online: 17 September 2010
© Springer Science+Business Media, LLC. 2010

Abstract Boron neutron capture therapy (BNCT) is based on the nuclear capture and fission reactions that occur when non-radioactive ^{10}B is irradiated with low energy thermal neutrons to produce α-particles ($^{10}B[n,\alpha]^{7}Li$). Carboranylporphyrins are a class of substituted porphyrins containing multiple carborane clusters. Three of these compounds, designated H_2TBP, H_2TCP, and H_2DCP, have been evaluated in the present study. The goals were two-fold. *First*, to determine their biodistribution following intracerebral (i.c.) administration by short term (30 min) convection enhanced delivery (CED) or sustained delivery over 24 h by Alzet™ osmotic pumps to F98 glioma bearing rats. *Second*, to determine the efficacy of H_2TCP and H_2TBP as boron delivery agents for BNCT in F98 glioma bearing rats. Tumor boron concentrations immediately after i.c. pump delivery were high and they remained so at 24 h. The corresponding normal brain concentrations were low and the blood and liver concentrations were undetectable. Based on these data, therapy studies were initiated at the Massachusetts Institute of Technology (MIT) Research Reactor (MITR) with H_2TCP and H_2TBP 24 h after CED or pump delivery. Mean survival times (MST) ± standard deviations of animals that had received H_2TCP or H_2TBP, followed by BNCT, were of 35 ± 4 and 44 ± 10 days, compared to 23 ± 3 and 27 ± 3 days, respectively, for untreated and irradiated controls. However, since the tumor boron concentrations of the carboranylporphyrins were 3–5× higher than intravenous (i.v.) boronophenylalanine (BPA), we had expected that the MSTs would have been greater. Histopathologic examination of brains of BNCT treated rats revealed that there were large numbers of porphyrin-laden macrophages, as well as extracellular accumulations of porphyrins, indicating that the seemingly high tumor boron concentrations did not represent the true tumor cellular uptake. Nevertheless, our data are the first to show that carboranyl porphyrins can be used as delivery agents for BNCT of an experimental brain tumor. Based on these results, we now are in the process of synthesizing and evaluating carboranylporphyrins that could have enhanced cellular uptake and improved therapeutic efficacy.

Keywords Convection enhanced delivery · Carboranylporphyrins · Boron neutron capture therapy · F98 rat glioma

W. Yang · R. F. Barth (✉) · G. Wu · T. Huo
Department of Pathology, The Ohio State University, 165 Hamilton Hall 1645 Neil Avenue, Columbus, OH 43210, USA
e-mail: rolf.barth@osumc.edu

P. J. Binns · K. J. Riley
Nuclear Reactor Laboratory, Massachusetts Institute of Technology, Cambridge, MA 02139, USA

O. Ongayi · V. Gottumukkala · M. G. H. Vicente
Department of Chemistry, Louisiana State University, Baton Rouge, LA 70803, USA

S. Kawabata
Department of Neurosurgery, Osaka Medical College, Takatsuki City, Osaka, Japan

Present Address:
P. J. Binns
Department of Radiation Oncology, Mount Auburn Hospital, Cambridge, MA 02138, USA

K. J. Riley
Radiation Monitoring Devices, Inc, Watertown, MA 02472, USA

Introduction

Boron neutron capture therapy is based on the nuclear capture and fission reactions that occur when non-radioactive boron-10 is irradiated with neutrons of the appropriate energy to yield high energy alpha particles (^{4}He) and recoiling lithium-7 (^{7}Li) nuclei. Since these particles have pathlengths of approximately one cell diameter, their lethality primarily is limited to boron containing cells. BNCT, therefore, can be regarded as both a biologically and a physically targeted type of radiation therapy. Its success is dependent upon the selective delivery of sufficient amounts of ^{10}B to cancer cells with only small amounts localized in the surrounding normal tissues. A wide variety of boron delivery agents have been synthesized [1], but only two of these currently are being used in clinically. The first, which has been used primarily in Japan, is sodium borocaptate or BSH, and the second is a dihydroxyboryl derivative of phenylalanine referred to as boronophenylalanine or BPA [2]. The latter has been used in clinical trials in Japan, Europe and the United States, primarily for the treatment of high grade gliomas, and more recently for recurrent tumors of the head and neck region. Following i.v. administration of either BPA or BSH by i.v. infusion, the tumor site is irradiated with neutrons, the source of which is a nuclear reactor.

Several recent clinical studies on the treatment of patients with glioblastomas (GBM) by means of BNCT have reported encouraging results [3–6]. Careful analysis of survival data from a study, carried out in Sweden [3] in which BPA was administered at a higher dose over a longer period of time [4], suggested that a subset of patients had survival times that were at least as good as those obtained with conventional therapy consisting of X-irradiation in combination with temozolomide (TMZ) [7]. Similarly, BNCT studies carried out by Miyatake and Kawabata and their co-workers [5, 6], in which BPA and BSH were administered in combination, followed by an X-ray boost [6] showed favorable responses in patients with newly diagnosed GBM and especially those in high risk groups [6]. However, a randomized Phase III clinical trial ultimately will be necessary to unequivocally establish that BNCT can produce equivalent or superior survival data compared to the current standard treatment of surgery followed by RT and TMZ. Interested readers are referred to the recently published proceedings of the Thirteenth International Congress on Neutron Capture Therapy for more detailed information relating to BNCT [8].

There has been a long-standing interest on the part of a number of research groups on the design, synthesis and biological evaluation of boron-containing porphyrins as delivery agents for BNCT [9–28]. Detailed information on this subject is provided in two comprehensive reviews on boronated porphyrins [21, 22]. The carboranylporphyrins used in the present study belong to a class of *meso*-substituted porphyrins containing four *nido*-carborane clusters and 36 boron atoms per molecule (37–31% boron by weight), linked to the porphyrin macrocycle *via* hydrolytically-stable carbon–carbon bonds. These compounds have been designated 5,10,15,20-tetra-(4-*nido*-carboranylphenyl)tetrabenzoporphyrin (H_2TBP), 5,10,15,20-tetra-(4-*nido*-carboranylphenyl)porphyrin (H_2TCP) and 5,15-di-[3,5-(*nido*-carboranylmethyl)phenyl]porphyrin (H_2DCP) and their structures are shown in Fig. 1. The synthesis and preliminary biological evaluation of H_2TCP [23–26], H_2DCP [26, 27] and H_2TBP [28, 29], previously have been reported. Earlier studies [23–25, 27–29] suggested that H_2TCP, H_2DCP and H_2TBP were promising boron delivery agents due to their low toxicity and enhanced tumor uptake.

Based on the reports of Ozawa et al. [30, 31] and our own experience with CED [32], we decided to focus on direct i.c. delivery of the carboranylporphyrins rather than

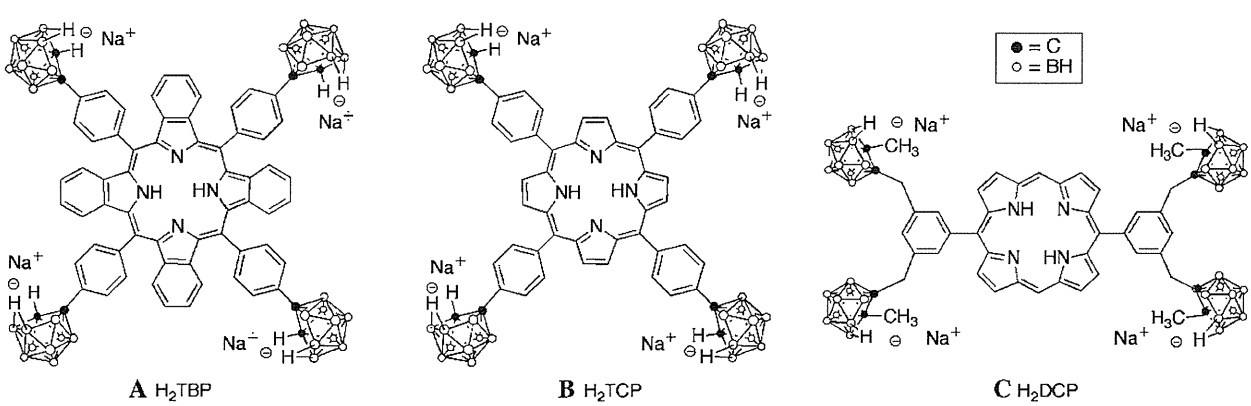

Fig. 1 Chemical structures of the carboranylporphyrins used in this study: **A** tetra(4-*nido*-carboranylphenyl)tetra-benzo-porphyrin, H_2TBP; **B** tetra(4-*nido*-carboranylphenyl) porphyrin (H_2TCP); and **C** di[3,5-(*nido*-carboranylmethyl)phenyl]porphyrin (H_2DCP)

systemic administration. CED is an innovative method for local drug delivery to brain tumors by which a pressure gradient, or bulk flow, is used to drive an infusate through the extracellular compartment [33]. It allows delivery of the infusate to the tumor and surrounding brain at much higher concentrations than could be achieved by systemic administration. As demonstrated in both animal studies [32, 34] and clinical trials [35, 36], CED not only increased the delivery of both low and high molecular weight agents, but also improved their therapeutic efficacy. Initially, we carried out some preliminary studies with several carboranylporphyrins using the F98 rat glioma model [37]. We now present a more detailed evaluation of the biodistribution and efficacy of H_2TCP, H_2DCP and H_2TBP as potential boron delivery agents for neutron capture therapy (NCT).

Materials and methods

Synthesis of carboranylporphyrins

All *nido*-carboranylporphyrins were synthesized from the corresponding *closo*-carboranylporphyrins via base-induced degradation for H_2TCP and H_2DCP or fluoride-induced degradation for H_2TBP [38]. Therefore, all of them were stereoisomers, as shown by ^{1}H-NMR spectra and ab initio calculations, which might contribute to their therapeutic efficacy. The percent boron by weight was 27% for H_2TBP and 31% for H_2TCP and H_2DCP. Two of these were converted to their zinc complexes, ZnDCP and ZnTCP, for the biodistribution studies described below. These were all stable for months at physiologic temperatures, but they were light sensitive and, therefore, they were shielded from light prior to their administration.

Biodistribution of ZnDCP and ZnTCP in glioma bearing mice

Biodistribution studies were carried out in female C57Bl/6 mice (Animal Production Branch, National Cancer Institute, Frederick, MD), weighing 20–25 g, bearing the syngeneic murine GL261 glioma. This tumor was induced by the i.c. implantation of methylcholanthrene pellets into the brain of a C57Bl/6 mouse [39]. It is composed of poorly differentiated cells histopathologically consistent with a glioblastoma. Tumor cells were implanted subcutaneously (s.c.) into the right dorsum with an inoculum of 1.8×10^6 cells. Biodistribution studies were carried out 15 days after implantation at which time the tumor volumes were ~ 80 mm^3. The zinc(II) complexes of H_2DCP and H_2TCP, ZnDCP and ZnTCP, respectively, were injected intraperitoneally (i.p.) over 8 h in three doses totaling 30 mg boron/kg body weight (b.w.). Since these compounds are photosensitizers, the animals were shielded from light during the course of the experiment. In order to compare their biodistribution with that of BPA, another group of mice received a single i.p. injection of BPA at a concentration of 500 mg/kg b.w. Mice were euthanized at 24 and 48 h following the first injection and tissue and blood samples were taken for boron determinations by means of direct current plasma-atomic emission spectroscopy (DCP-AES), as previously described by us [40]. All animal studies were done in accordance with the *Guide for the Care and Use of Laboratory Animals* (National Academy Press, Washington, DC, 1996) and the protocol was approved by the Institutional Laboratory Animal Care and Use Committee of The Ohio State University.

F98 rat glioma model

The F98 rat glioma (#CRL-2397, American Type Culture Collection, Manasus, VA) was derived from an undifferentiated neoplasm transplacentally induced in the progeny of a pregnant CD Fischer rat by the i.v. administration of *N*-ethyl-*N*-nitrosourea [41]. It has been propagated in vitro and in vivo since 1971 and, as described in a recent review [42], the F98 glioma has been used in a wide variety of studies in experimental neuro-oncology. This tumor has an infiltrative pattern of growth within the brain, and an i.c. inoculum of as few as ten cells can be fatal. In the present study, F98 cells were grown in Dulbecco's modified Eagle's medium (DMEM) (Gibco, Grand Island, NY) supplemented with 10% fetal bovine serum (FBS) (Hyclone, Logan, UT), 100 units/ml penicillin, 100 μg/ml streptomycin and 2 mM L-glutamine. Fischer rats (Animal Production Branch, National Cancer Institute, Frederick, MD), weighing 220–240 g, were used in these studies. A stereotactic implantation procedure, which has been described in detail elsewhere, was employed [43]. Briefly, rats were sedated by i.p. administration of a 1.2:1 mixture of ketamine/xylazine at a dose of 120 mg of ketamine/20 mg xylazine/kg b.w. Following this, a small burr hole was drilled into the calvarium and a plastic screw with an entry port (Arrow Machine Manufacturing, Inc., Richmond, VA) was embedded into the skull. F98 cells at a concentration of either 10^3 for therapy studies or 10^5 cells for biodistribution studies were injected stereotactically into the right caudate nucleus over 10–15 s through a small entry port of the plastic screw. Following this, the entry port was filled with bone wax immediately after withdrawal of the needle, and the operative field was flushed with betadine before the scalp incision was closed with a single sterilized clip. Eleven to thirteen days after tumor implantation of 10^5 cells, when clinical signs of a progressively growing i.c. tumor were evident, biodistribution studies were initiated.

Biodistribution studies in F98 glioma bearing rats following convection-enhanced delivery (CED) of carboranylporphyrins

Since the zinc(II) complexes of carboranylporphyrins had lower cellular uptake than the free base porphyrins, studies subsequently were carried out with H_2DCP and H_2TCP. In order to increase tumor uptake and decrease uptake by extracranial organs and tissues, these were administered i.c. by means of CED or Alzet^{TM} pump infusion to F98 glioma bearing rats. Eleven to thirteen days after tumor implantation, when signs of a progressively growing i.c. tumor were evident (weight loss, lethargy, hunching, and ataxia), biodistribution studies were initiated. In contrast to the biodistribution studies carried out in mice, which had received the test porphyrins by i.p. injection, it was not necessary to shield these rats from light. For short term CED of the carboranylporphyrins, a 28 gauge needle was inserted into the entry port of the plastic screw and then advanced 5 mm below the dura into the tumor. The boronated porphyrins were diluted with phosphate buffered saline (PBS), pH 7.4, to yield a concentration of 0.1–0.2 mg of compound in 10 μl. They compounds were administered by CED at a flow rate of 0.33 μl/min for 30 min using a syringe pump (Harvard Apparatus Co, Cambridge, MA). Biodistribution was determined immediately after and 24 and 48 h after termination of CED. Animals were euthanized by an overdose of halothane, following which tumors and normal tissues, consisting of brain, blood, liver, kidney and muscle, were removed and weighed. Uptake of boron was quantified by means of DCP-AES [40].

Biodistribution of carboranylporphyrins following i.c. infusion by osmotic pumps

Alzet osmotic pumps (model #2001 D) and brain infusion kits (rigid stainless-steel cannula, 7 mm, 28 gauge) were assembled and filled with 200 μl of the test carboranylporphyrins. The pumps were stored in the dark in a sterile solution of 0.9% saline at 37°C for 24 h prior to their use. Fourteen days after tumor implantation, the rats were anesthetized again and the scalp was reopened. The pumps were implanted s.c. between the scapulae. The infusion cannula and needle were inserted stereotactically into the entry port of the plastic screw and the needle was advanced 5 mm below the dura into the tumors of glioma bearing rats. H_2DCP, H_2TCP or H_2TBP at varying doses, ranging from 0.2 to 1.0 mg, were delivered in volume of 200 μl at a constant flow rate of 8 μl/h over 24 h following which the animals were euthanized immediately (t = 0) or 24 or 48 h later. Boron concentrations were determined in samples of tumor, brain, blood, liver, spleen, kidneys, lungs and heart by means of DCP-AES.

Therapy experiments

BNCT was performed 14 days following stereotactic implantation of 10^3 F98 glioma cells. Rats were transported to the Nuclear Reactor Laboratory at the Massachusetts Institute of Technology (MIT). Based on the results of the biodistribution study, a total of either 0.2 mg of the compound was administered by CED for 30 min or 0.5 mg of the compound was infused for 24 h by Alzet pumps. The animals were then randomized on the basis of weight into experimental groups of 9–10 animals each as follows: Group 1, H_2TCP, administered by Alzet pumps and BNCT; Group 2, H_2TBP by Alzet pumps and BNCT; Group 3, H_2TBC by CED and BNCT; Group 4, H_2TBP by CED + i.v. BPA and BNCT; Group 5, i.v. BPA, followed 2.5 h later by BNCT; Group 6, CED of saline and neutron irradiation; Group 7, unirradiated controls that received H_2TCP by CED. BNCT was initiated 24 h after termination of CED or infusion and 2.5 h after i.v. administration of ^{10}B enriched BPA at a dose of 500 mg/kg b.w. (Ryscor Science, Inc., Raleigh, NC). All irradiated rats were anesthetized with a mixture of ketamine and xylazine. BNCT was carried out at the MITR-II nuclear reactor in the M011 irradiation facility. This produces a beam of thermal neutrons of high purity and intensity with no measurable fast neutron component. Two rats at a time were positioned in a ^{6}Li enriched polyethylene box that provided whole body shielding from the thermal neutrons during an irradiation. The animals' heads were aligned in the middle of a 13 × 2 cm^2 aperture, which served as the beam collimator. Four fission counters, located at the periphery of the 15 cm circular field automatically controlled beam delivery and provided real time data on the relative neutron fluence during an irradiation.

Dosimetry

After completion of BNCT, the animals were held at MIT for ~3 days to allow induced radioactivity to decay before they were returned to The Ohio State University for clinical monitoring. Dosimetric measurements were performed using bare gold foils and a graphite walled ionization chamber (V = 0.1 cm^3) flushed with reagent grade CO_2 on both dead rats and phantoms made from type 6 nylon [44]. The measured dose rates in brain (2.2% nitrogen by weight), normalized to the reactor operating at a power of 5 MW, were 18.5 cGy/min for photons, 7.7 cGy/min for thermal neutrons from the nitrogen capture reaction and 3.4 cGy/min per μg ^{10}B in tissues. For dosimetric calculations, boron concentrations were determined in tumor, normal brain, liver and blood in a separate group of animals 24 h after CED of carboranylporphyrins and 2.5 h after i.v. injection of BPA. Animal irradiations were

performed with the reactor operating at a power between 4.0 and 4.8 MW, and these took approximately 7 min to deliver a thermal neutron fluence of 2.64×10^{12} n.cm^{-2} to complement previous dose prescriptions [45].

Monitoring of clinical status and neuropathologic evaluation

All animals were weighed three times per week and their clinical status was evaluated at the same time. Once the animals had progressively growing tumors, as evidenced by the combination of sustained weight loss, ataxia and peri-orbital hemorrhage, they were euthanized in order to minimize discomfort. Survival times were determined by adding 1 day to the time between tumor implantation and euthanization. The brains of all animals in the therapy studies were removed after death, fixed in 10% buffered formalin, and then cut coronally at the level of the optic chiasm and 2 mm anterior and posterior to it. Tissue sections through the tumor were embedded in paraffin, cut at 4 μm, stained with hematoxylin and eosin (H&E), and examined microscopically to assess the histopathologic changes.

Statistical evaluation

The means and standard deviations (SD) were computed for boron concentrations in all the major organs of C57Bl/6 mice bearing s.c. implants of the GL261 murine glioma, as described in Table 1, and for the tumor, brain, and blood of the F98 glioma rats, as described in Table 2. Tumor:-brain and tumor:blood boron concentration ratios were calculated for each group. To study the effects of BNCT on survival of F98 glioma bearing rats, the mean survival time

Table 1 Boron biodistribution in tumor and normal tissue following i.p. injection of either ZnDCP or ZnTCP in mice bearing s.c. implants of the GL261 murine glioma

Agent[a]	Time (h)	Boron concentrations ± SD (μg/g)[b]						Ratios[c]	
		Tumor	Brain	Blood	Liver	Spleen	Muscle	T/Br	T/Bl
ZnDCP	24	8.3 ± 2.7	1.7 ± 0.8	44.5 ± 12.6	94.7 ± 7.3	109.4 ± 10.0	10.9 ± 6.6	4.8	0.2
	48	7.6 ± 1.9	1.2 ± 0.4	15.9 ± 3.5	154.9 ± 28.4	138.5 ± 60.1	6.7 ± 3.2	6.3	0.5
ZnTCP	24	2.0 ± 0.1	0.7 ± 0.6	25.5 ± 31.1	43.1 ± 4.8	115.9 ± 73.6	1.5 ± 0.2	2.6	0.1
	48	5.2 ± 0.3	0.5 ± 0.1	11.3 ± 2.5	46.3 ± 11.5	114.0 ± 99.1	3.0 ± 0.1	10.4	0.5
BPA	2.5	12.5 ± 4.1	1.0 ± 0.2	2.6 ± 0.8	1.1 ± 0.2	3.2 ± 1.9	1.1 ± 0.6	12.5	4.8

[a] ZnDCP or ZnTCP was administered by 3 i.p. injections, administered over 8 h to C57BL/6 mice bearing s.c. implants of the GL261 murine glioma. Animals were euthanized at 24 and 48 h following the third injection and tissues and blood samples were removed for boron determinations. BPA was administered i.p. at a dose of 25 mg b/kg b.w. and mice were euthanized 2.5 h later

[b] Boron concentrations were determined by DCP-AES. The mean boron values (μg/g wt of tissue) ± the standard deviation are shown for groups of four animals

[c] T:Br indicates the tumor to normal brain ratio and T:Bl indicates the tumor to blood ratio

Table 2 Boron biodistribution in F98 glioma bearing rats following administration of escalating doses of H_2TCP by osmotic pumps

Dose (mg/200 μl)	Time (h)	Boron concentration ± SD (μg B/g)[a]			Ratios[b]	
		Tumor	Brain	Blood	T:Br	T:Bl
0.2	0	18.7 ± 8.7	1.3 ± 1.0	0.3 ± 0.3	14.0	64.7
	24	24.6 ± 5.1	2.9 ± 2.7	0.5 ± 0.7	8.5	54.1
	48	9.0 ± 2.7	0.5 ± 0.5	0.3 ± 0.1	18.0	31.9
0.5	0	88.4 ± 20.2	2.0 ± 0.9	0.4 ± 0.2	45.2	207.6
	24	102.9 ± 26.3	3.3 ± 4.1	0.5 ± 0.1	31.3	196.0
	48	16.8 ± 8.4	0.3 ± 0.1	0.3 ± 0.1	49.9	50.5
1.0	0	123.3 ± 61.1	6.5 ± 3.8	0.2 ± 0.1	18.9	593.3
	24	149.6 ± 55.5	10.1 ± 12.6	0.2 ± 0.1	14.8	708.8
	48	34.8 ± 10.8	3.0 ± 1.9	0.3 ± 0.1	11.5	105.5

[a] H_2TCP (0.2–1.0 mg) was administered by means of Alzet osmotic pumps (#2001D) over 24 h to Fischer rats bearing i.c. implants of the F98 glioma. Animals were euthanized at different time point (0, 24, 48 h after termination) and tissues and blood samples were removed for boron determinations by DCP-AES. The values indicated are means ± SD for groups of four to five rats

[b] T:Br indicates the tumor to normal brain ratio of the ipsilateral cerebral hemisphere and T:Bl indicates the tumor to blood ratio

(MST), SD, and median survival time (MeST) were calculated for each group using the Kaplan–Meier estimate [46]. Kaplan–Meier curves also were plotted for all groups. An overall log rank test was performed to test for equality of survival curves over the groups. Wald tests were used for individual comparisons between two groups, with a Bonferroni method of adjustment for multiple comparisons [47]. Since there was no censoring of the survival data, a two sample t test also was used to compare MSTs in order to increase the power of the test. The percent increased life span (% ILS) was determined from the following equation:

$$\%\mathrm{ILS} = \frac{\mathrm{MeST(orMST)_t} - \mathrm{MeST(orMST)_u}}{\mathrm{MeST(orMST)_u}} \times 100$$

where "t" designates treated and "u" designates untreated animals.

Results

Biodistribution after systemic injection of carboranylporphyrins

Following i.p. injection of either ZnDCP or ZnTCP (30 mg B/kg b.w.) to GL261 tumor bearing mice, one of five animals in each group died within the first 24 h and the others demonstrated reduced activity, suggesting that these doses of the zinc complexes were toxic. In contrast, H_2DCP and H_2TCP previously were shown to have very low toxicity [27, 28]. The boron uptake in tumor and normal tissues at 24 and 48 h following the third i.p. injection are summarized in Table 1. The tumor boron concentrations at 48 h were 7.6 ± 1.9 and 5.2 ± 0.3 μg/g of tissue for ZnDCP and ZnTCP, respectively, compared to 1.2 ± 0.4 and 0.5 ± 0.1 μg/g in normal brain. In contrast, the 48 h boron concentrations in the liver were 154.9 ± 28.4 and 46.3 ± 11.5 μg/g, respectively, and the spleen concentrations were 138.5 ± 60.1 and 114.0 ± 99.1 μg/g with marked animal to animal variability. This possibly reflected differences in the excretion of the compounds and their metabolites. The corresponding blood concentrations were 15.9 ± 3.5 and 11.3 ± 2.5 μg/ml, respectively. Based on these data, a decision was made to administer the carboranylporphyrins i.c. either by short term (30 min) CED or by a 24 h infusion using Alzet osmotic pumps. In contrast to the high extracranial tissue uptake of ZnDCP and ZnTCP, BPA had very low concentrations in all organs except for tumor (12.5 ± 4.1 μg/g).

Biodistribution following delivery of carboranylporphyrins by either CED or Alzet pumps

As shown in Tables 2 and 3, administration by either Alzet pumps or CED resulted in higher tumor and lower normal tissue boron concentrations, and improved tumor:brain (T:Br) and tumor:blood (T:Bl) ratios compared to those obtained following i.p. injection (Table 1). The boron concentrations in tumor and selected normal tissues in F98 glioma bearing rats following Alzet pump delivery of H_2TCP at doses of 0.2, 0.5 or 1.0 mg/200 μl, delivered i.c. into F98 glioma bearing rats are summarized in Table 2. Tumor boron concentrations were clearly dose dependent immediately following infusion and at 24 and 48 h later. The highest tumor boron concentrations were observed at 24 h following administration of escalating doses of H_2TCP (24.6, 102.9 and 149.6 μg/g), but these were all within 1 SD of the concentrations that were observed immediately following infusion, indicating that there was retention and possibly some accretion of boron within the tumor. In contrast, the tumor concentrations had fallen

Table 3 Boron concentrations and physical radiation doses delivered in F98 glioma bearing rats 24 h following administration of carboranylporphyrins by osmotic pumps or CED

Agent/route[a]	Boron concentrations (μg/g)[b]			Physical radiation dose[c]		
	Tumor	Brain	Blood	Tumor	Brain	Blood
H_2TCP/pump	102.9 ± 26.3	3.3 ± 4.1	0.7 ± 0.9	25.4	2.5	1.9
H_2TBP/pump	61.9 ± 16.4	0.8 ± 0.9	0.2 ± 0.4	16.0	1.9	1.8
H_2DCP/pump[d]	35.6 ± 9.0	5.2 ± 6.8	0.5 ± 0.5	9.9	2.9	1.9
H_2TBP/CED	140.3 ± 70.9	0.8 ± 0.3	0.2 ± 0.1	34.0	1.9	1.8

[a] H_2DCP, H_2TCD and H_2TBP at doses of 0.5 mg were administered to Fischer rats bearing i.c. implants of the F98 glioma by Alzet osmotic pumps or at a dose of 0.2 mg by CED. The animals were euthanized 24 h after administration and tissues and blood samples were taken for boron determinations

[b] Boron concentrations were determined in samples of tumor, brain, blood, liver, spleen, kidneys, lung and heart, by means of direct current plasma-atomic emission spectroscopy. Except as indicated above, boron concentrations were at the undetectable level (<0.5 μg/g) in all other tissues. The values indicated are means ± standard deviation for groups of four to five rats

[c] Physical dose estimates include contributions from gamma photons, ^{14}N (n,p), ^{14}C and ^{10}B (n,α) ^{7}Li reactions

[d] Based on the low tumor boron values and the calculated physical radiation doses, BNCT was not carried out using H_2DCP